# Delivering Smooth Power to Pulse-Current Battery Chargers: Electric Vehicles as a Case in Point

Mahdi Bayati, Mehrdad Abedi, *Member, IEEE*, Maryam Farahmandrad,
and Gevork B. Gharehpetian, *Senior Member, IEEE*

***Abstract*—This article proposes a battery charger for electric vehicles based on pulse-current charging method which has great distinct advantages and substantially enhances charging process. It applies positive, negative, and zero currents for each cycle. On the one hand, drastic changes in the battery current and power during the cycles appear in the output of the battery charger, negatively affect the terminal, and frequently change the output active power. This condition is also important in battery chargers which do not have dc–ac stage and are powered by other power sources, for instance, fuel cell. On the other hand, the output active and reactive powers must track constant values without any variations for participation in vehicle-to-grid technology. Thus, a particular parallel battery–capacitor topology is suggested in practice and then an innovative control system is precisely designed in order to implement pulse-current method and transfer smooth power in the presence of the intrinsic drastic changes in the battery power. The proposed system is compared with the recent pulse-current battery chargers. The results demonstrate the effectiveness of the solution. This article is accompanied by a PDF file demonstrating the details.**

***Index Terms*—Battery charger (BC), charging method, dc–dc converter, electric vehicle (EV), pulse current.**

## NOMENCLATURE

| | |
|---|---|
| $T_p$ | Positive pulse period in pulse current. |
| $T_n$ | Negative pulse period in pulse current. |
| $T_r$ | Rest period in pulse current. |
| $I_0$ | Amplitude of pulse current. |
| $f_{\text{sw}}$ | Switching frequency. |
| $v_{\text{oc}}$ | Open-circuit battery voltage measured during $T_r$. |
| $V_0$ | Maximum permissible battery voltage. |
| $^*$ | Symbol of a reference command. |
| $v_{0p}$ | Capacitor voltage at the beginning of $T_p$. |
| $v_{0n}$ | Capacitor voltage at the beginning of $T_n$. |
| $v_{0r}$ | Capacitor voltage at the beginning of $T_r$. |
| $d_B$ | Duty Cycle for the leg $Q_7Q_8$. |
| $d_C$ | Duty Cycle for the leg $Q_9Q_{10}$. |
| $\tau_f$ and $\tau'_f$ | Time constants of the sensors. |
| $k'_p$, $k'_i$, $k''_i$, and $k''_p$ | Parameters of the controllers. |

## I. INTRODUCTION

NOWADAYS, battery chargers (BCs) of electric vehicles (EVs) have attracted a great deal of attention. They are designed based on a high-quality charging–discharging method in order to improve the battery performance and lifetime. A particular current or a particular voltage must be imposed on the battery in order to charge or discharge. Charging methods for batteries can be categorized according to the voltage or current waveform regardless of charging profile or algorithm into constant-current constant-voltage (CC-CV) [1], pulse current [2]–[5], Reflex [6]–[12], pulse voltage [13]–[16], and sinusoidal ripple current [17], [18]. Reflex method applies a pulse current with a short negative pulse current, so it is sometimes called pulse-current method. Pulse-current method in general applies positive, negative, and zero currents for each cycle. This three-stage sequence includes $T_p$, $T_n$, and $T_r$. Since pulse voltage leads to pulse current in the battery impedance, pulse-voltage method can be also considered as a type of pulse-current method.

Pulse-current method in general is widely used in advanced battery systems because it enables the chemical reactions to keep pace with the charging process, stabilizes the chemical reactions, diffuses and neutralizes the electrolyte density, eliminates the concentration polarization, increases the power transfer rate, decreases the charging time, reduces the internal temperature, and improves the charging efficiency [2]–[16]. Accordingly, it enhances the overall charging process. Therefore, this article focuses on pulse-current method.

As a consequence of the drastic battery current changes in pulse-current method, the drastic battery power changes appear in the output of the EV BC, negatively affect the terminal, and frequently change the output active power. This unfavorable condition may also occur in BCs which do not have dc–ac stage and are powered by dc distribution networks [19] or other power sources, for instance, fuel cell [20], [21]. On the other hand, the output active and reactive powers must track constant values without any variations for participation in vehicle-to-grid (V2G) technology like what have been proposed in [22], [23].

---

Manuscript received February 9, 2020; revised May 16, 2020; accepted June 25, 2020. Date of publication July 1, 2020; date of current version September 22, 2020. Recommended for publication by Associate Editor F. J. Azcondo. *(Corresponding author: Mahdi Bayati.)*

Mahdi Bayati, Mehrdad Abedi, and Gevork B. Gharehpetian are with the Department of Electrical Engineering, Amirkabir University of Technology, Tehran 15875-4413, Iran (e-mail: bayati.mahdi@aut.ac.ir; abedi@aut.ac.ir; grptian@aut.ac.ir).

Maryam Farahmandrad is with the Department of Electrical Engineering, Bu-Ali Sina University, Hamedan 6516738695, Iran (e-mail: m.farahmandrad@alumni.basu.ac.ir).

This article has supplementary downloadable material available at https://ieeexplore.ieee.org, provided by the authors.

Color versions of one or more of the figures in this article are available online at https://ieeexplore.ieee.org.

Digital Object Identifier 10.1109/TPEL.2020.3005929

Thus, particular importance should be given to this power quality problem. In this regard, there are some important works [6], [7], [12], [20], [21], [24], [25].

The purpose of this article is to propose an EV BC based on pulse-current method which is able to participate in V2G technology without the mentioned power quality problem. In other words, it receives smooth constant power and charges the battery based on pulse-current method, and also the output active and reactive powers track constant values without any variations in the presence of the drastic battery power changes.

## II. RESEARCH CONTRIBUTION

### A. Charging and Discharging

As previously mentioned, some research studies have been conducted on sharing smooth power between multiple battery packs or branches [12], [20], [21], [24], [25]. Pulse-current method without the negative pulse current is considered in [20], [21], and [24], while pulse-current method with the negative part is considered in this article. Frequency and duty cycle of the pulse currents in [20], [21], and [24] are dependent on each other, but the proposed system can freely work in adjusted frequency and duty cycle. This issue becomes important when the frequency and duty cycles are adaptively tuned during optimal charging process [13], [14], [16]. In this article, a general waveform for the battery current has been considered. $T_p$, $T_n$, $T_r$, and $I_0$ can reach desired values of even zero and then be given to the control system as reference commands. Obviously, pulse-current method without the negative pulse is made if $T_n$ equals zero. CC method is made if both $T_r$ and $T_n$ equal zero. Discharging can be also obtained if $T_p < T_n$ or $T_p = 0$. The capability to adjust all the parameters of pulse-current method can be a great achievement in this article.

The concepts introduced in [12], [20], [21], [24], and [25] are about multiple battery packs or branches. Thus, they are not useful when a single battery pack is supposed to be charged, for instance, when a single EV is connected to a microgrid through its port in a charging station. But, this article is not confined to using multiple battery packs.

The general generated voltage and current waveforms can implement many algorithms or charging profiles, for instance, multi-stage CC-CV. In [26], eight distinct algorithms have been compared. Interestingly, the control system introduced in this article is able to implement all of them through a high-power topology.

This article focuses on the dc–dc stage of the EV BC. But, it can be used in many applications instead of dc–dc stage of various BCs such as the fuel-cell-powered BCs in [20] and [21], the multi-output BCs in [12], [24], and [25], and the charging stations in [19] to share smooth constant power.

Despite the negative pulse current in pulse-current method being still underway for Li-ion batteries [9]–[11], [26], a general concept has been developed. But it is definitely advantageous for lead–acid batteries [6], [7], [12] (please refer to the bibliographies of [6], [7], [9]–[12], and [26] as well). $T_n$ can be zero in the theory presented in this article and the BC can be redesigned for different battery types and specifications, considering all challenging technical issues.

### B. Electrochemical Impedance Spectroscopy

Pulse-current waveform also has another application in electrochemical impedance spectroscopy (EIS) [27]–[29]. The EIS is a powerful analysis to measure the parameters such as state of health and state of charge [30]. Online EIS is divided into some categories [30]. One of them focuses on measurement through power electronics converters [27], [30]–[32]. The one in [27] concerns a method for online EIS which employs a closed-loop control system generating pulse-current waveforms in a half-bridge converter. In addition to the main purpose, the proposed closed-loop control system can be utilized in order to generate pulse-current waveforms, suitable for advanced online EIS algorithms, in a controlled way, while the idea in [27] is based on perturbation. Perturbation, especially in a wide range of frequencies, threatens the stability.

## III. SYSTEM DESCRIPTION

### A. Power Electronics Topology

Fig. 1 proposes the configuration of the EV BC. The dc–ac stage with its control system regulates $Q_s$ at $Q_s^*$ and $v_{\mathrm{dc}}$ at $v_{\mathrm{dc}}^*$ to make a regulated dc link for the dc–dc stage in a predetermined power factor. The dc–ac stage and its control system is very well known and widely studied in many recent works [33]. Therefore, it is not worth studying again and this article focuses on only the dc–dc stage.

The dc–dc stage is similar to a type of hybrid energy storage system, parallel active battery–capacitor configuration [34]. This stage with its control system imposes pulse-current method on the Li-ion battery and resolves the power quality problem caused by the drastic battery current changes in pulse-current method. The first duty is done by the leg $Q_7Q_8$ and the second duty is done by the leg $Q_9Q_{10}$. Fig. 2 shows the whole control system. The second control loop in Fig. 2 regulates $i_B$ at $i_B^*$ by means of the leg $Q_7Q_8$ and the third control loop regulates $i_C$ at $i_C^*$ by means of the leg $Q_9Q_{10}$ until the battery voltage reaches the maximum permissible voltage $V_0$. Then, the first control loop regulates the battery voltage $v_B$ at $v_B^*$ by means of the leg $Q_7Q_8$. In other words, the two legs work as independent current sources until the battery reaches $V_0$. Then, the leg $Q_7Q_8$ works as a voltage source whose magnitude equals $V_0$ and the leg $Q_9Q_{10}$ is completely turned OFF. This charging algorithm is just an example like the algorithms proposed in [26]. The capacitor $C'$, shown in color in Fig. 1, is connected in parallel with the battery only when the leg $Q_7Q_8$ works as a voltage source. $d_B$ and $d_C$ generated by the voltage and control loops are inserted into the outputs column. Eventually, the switching functions of $Q_7$, $Q_8$, $Q_9$, and $Q_{10}$ are generated according to $d_B$ and $d_C$ with the switching frequency $f_{\mathrm{sw}}$. There are proportional–integral controllers which generate the control signals. They are passed through the saturation limiters (0 to 1). Then, they are divided

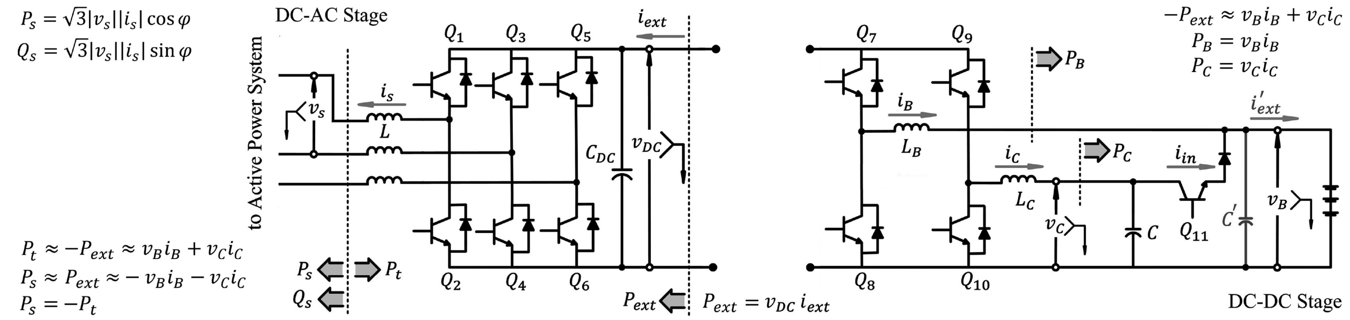

Fig. 1. Power electronic topology.

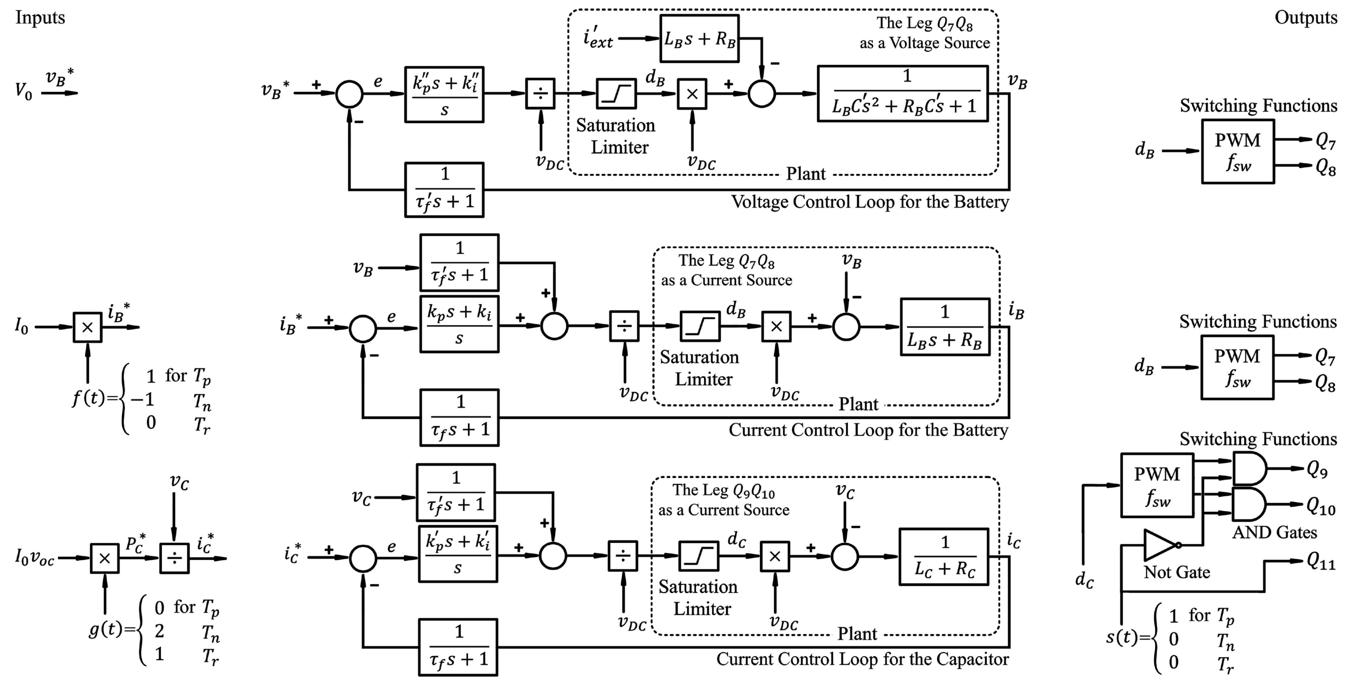

Fig. 2. Inputs, outputs, and control loops of the control system with modeling of the plants.

by $v_{\mathrm{dc}}$ to make the loops independent of $v_{\mathrm{dc}}$. Feed-forward compensation, adding $v_B$ and $v_C$ to the control signals in the second and third loops, has three great benefits [33]. The voltages and currents are measured using the sensors modeled in the form of the first-order transfer functions.

$i_B$ and $i_C$ are set to $i_B^*$ and $i_C^*$ by the control system until the battery reaches $V_0$. Then, $v_B$ is set to $v_B^*$. So, there are three reference commands which are necessary to be defined during $T_p$, $T_n$, and $T_r$. They have been defined in the inputs column of Fig. 2 in the block diagram forms. Additionally, the reference commands have been defined in the first and second rows of Table I in the mathematical forms. The inputs column of Fig. 2 generates the sequence of $i_B^*$ from multiplying $I_0$ by the function $f(t)$. Then, $i_B^*$ is given to the second control loop. It also generates $i_C^*$ from multiplying $I_0 v_{\mathrm{oc}}$ by the function $g(t)$ and then dividing the result by $v_C$ to make the sequence of $i_C^*$ defined in the second row of Table I. Finally, $i_C^*$ is given to the third control loop.

## *B. Operation Stages*

Fig. 3 shows the operation stages during the periods of pulse-current method. It has been sketched based on the values of $i_B^*$ and $i_C^*$ listed in Table I. Fig. 3 and the first row of Table I clearly show that the battery is charging based on pulse-current method. The control system applies the functions $f(t)$, $g(t)$, and $s(t)$ to generate the sequences of the reference commands. Table I is the heart of this article. There is a great interesting point in Table I. The third row shows the sequence of $P_B$ which equals $v_B i_B$. The open-circuit battery voltage $v_{\mathrm{oc}}$ approximately equals the terminal battery voltage $v_B$ if the battery impedance and its voltage drop are neglected. It approximately equals $I_0 v_{\mathrm{oc}}$ during $T_p$, $-I_0 v_{\mathrm{oc}}$ during $T_n$, and zero during $T_r$. It has the drastic changes as expected because pulse-current method is imposing on the battery. The fourth row shows the sequence of $P_C$ which equals $v_C i_C$. The sixth row shows the sequence of $P_B + P_C$ which does not change during $T_p$, $T_n$, and $T_r$. It equals $I_0 v_{\mathrm{oc}}$ during all the periods. Being constant and continuous (without

TABLE I
SEQUENCE OF SOME VARIABLES IN PULSE-CURRENT METHOD

| No. | Variable | $T_p$ | $T_n$ | $T_r$ |
|---|---|---|---|---|
| 1 | $i_B^*$ | $I_0$ | $-I_0$ | 0 |
| 2 | $i_C^*$ | 0 | $2I_0v_{oc}/v_C$ | $I_0v_{oc}/v_C$ |
| 3 | $P_B$ | $I_0v_B \approx I_0v_{oc}$ | $-I_0v_B \approx -I_0v_{oc}$ | 0 |
| 4 | $P_C$ | 0 | $2I_0v_{oc}$ | $I_0v_{oc}$ |
| 6 | $P_B + P_C$ | $I_0v_{oc} + 0 = I_0v_{oc}$ | $-I_0v_{oc} + 2I_0v_{oc} = I_0v_{oc}$ | $0 + I_0v_{oc} = I_0v_{oc}$ |
| 5 | $Q_{11}$ | On | Off | Off |
| 7 | Equations | $i_{in} = \frac{v_C - v_{oc}}{R_t} = -C\frac{dv_C}{dt}$ | $i_C = \frac{2I_0v_{oc}}{v_C} = C\frac{dv_C}{dt}$ | $i_C = \frac{I_0v_{oc}}{v_C} = C\frac{dv_C}{dt}$ |
| 8 | Solutions | $v_C = v_{oc} + \left(v_{0p} - v_{oc}\right)\exp\left(\frac{-t}{R_tC}\right)$ | $v_C = \left(\frac{4I_0v_{oc}}{C}t + v_{0n}^2\right)^{0.5}$ | $v_C = \left(\frac{2I_0v_{oc}}{C}t + v_{0r}^2\right)^{0.5}$ |
| 9 | Initial Voltages | $v_{0p} = \left[\frac{2I_0v_{oc}}{C}T_r + \frac{4I_0v_{oc}}{C}T_n + \left(v_{oc} + (v_{0p} - v_{oc})\exp\left(\frac{-T_p}{R_tC}\right)\right)^2\right]^{0.5}$ | $v_{0n} = \left[\left(\frac{2I_0v_{oc}}{C}T_r + \left(\frac{4I_0v_{oc}}{C}T_n + v_{0n}^2\right)\right)^{0.5} - v_{oc}\right]\exp\left(\frac{-T_p}{R_tC}\right) + v_{oc}$ | ×<br>× |

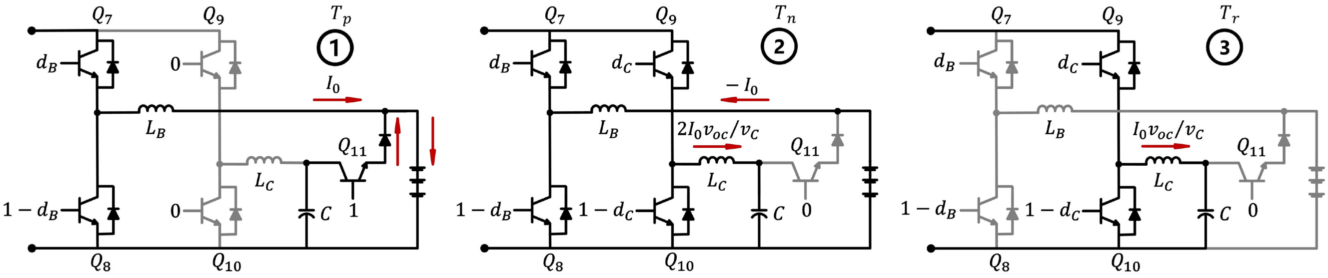

Fig. 3. Operation stages of the dc–dc stage shown in Fig. 1.

drastic changes and interruption) reveals a great achievement. The battery power ($P_B$) significantly changes during $T_p$, $T_n$, and $T_r$, while sum of the battery power and the capacitor power ($P_B + P_C$) do not change during $T_p$, $T_n$, and $T_r$. In other words, smooth power ($I_0v_{oc}$) is transferred from the dc–dc stage to the dc–ac stage and vice versa. In fact, the innovative allocation of $i_C^*$ and $P_C$ in accordance with the rule defined in Table I resolves the power quality problem, that is, $P_B + P_C$ remains constant and continuous (smooth) during $T_p$, $T_n$, and $T_r$.

As stated in Table I, the positive values for $P_C$ during $T_n$ and $T_r$ lead to increase in $v_C$ because it only receives power during each cycle. If this stored energy is not released, $v_C$ increases more and more and, eventually, it exceeds $v_{\rm dc}^*$ and the leg $Q_9Q_{11}$ does not work because it is a step-down dc–dc converter. There is only one opportunity to release that energy, only during $T_p$. Thus, $Q_{11}$ is turned ON during $T_p$ when the battery is being charged by $I_0$ (see Fig. 3 and the fifth row in Table I). $i_C$ and $i_B$ are controlled by the closed-loop control system, but $i_{\rm in}$ is not controlled. As shown in Fig. 3, $i_{\rm in}$ flows in only one direction because there is a diode in that branch and flows only when $v_C$ becomes more than $v_B$ and $Q_{11}$ is ON. The value of the current $i_{\rm in}$ depends on the voltage difference between $v_C$ and $v_B$ as well as the sum of resistances of the ON-state switch and the wires denoted by $R_t$. The diode blocks $I_0$ flowing to the battery during $T_p$. The battery is charged by the sum of two currents, $I_0$ and $i_{\rm in}$. Fig. 2 assigns the function $s(t)$ to $Q_{11}$ in order to make the sequence of the state of $Q_{11}$. $s(t)$ is toggled to turn OFF $Q_9$ and $Q_{10}$ simultaneously during $T_p$. It ensures that the leg $Q_9Q_{10}$ is completely turned OFFduring $T_p$.

### C. Ripple and Stability of $v_C$

The seventh, eighth, and ninth rows of Table I show the equations related to the capacitor $C$, the solutions to them, and the initial voltages of the capacitor $C$. Each period has a particular electrical circuit as depicted in Fig. 3. The seventh row contains the basic equations based on KVL and KCL laws for each electrical circuit. It is a fact that capacitor voltage is continuous. Therefore, the capacitor voltage at the beginning of each period must be equal to the capacitor voltage at the end of the previous period. The voltage difference between $v_{0p}$ and $v_{0n}$ is the voltage ripple.

From the standpoint of energy, the capacitor energy is an index for its voltage stability. For the stability

$$\int^{T_n} P_C dt + \int^{T_r} P_C dt \leq \int^{T_p} v_C i_{\rm in} dt. \tag{1}$$

This means that the released energy during $T_p$ must be equal to or more than the stored energy during $T_n$ and $T_r$. In steady-state condition for each cycle, the left side of (1) becomes equal to the right side. Therefore

$$2I_0 v_{\mathrm{oc}} T_n + I_0 v_{oc} T_r = \int_0^{T_p} \left[ v_{\mathrm{oc}} + (v_{0p} - v_{\mathrm{oc}}) \exp\left( \frac{-t}{R_t C} \right) \right] \frac{v_C - v_{\mathrm{oc}}}{R_t} dt. \quad (2)$$

This is a good index to judge the stability of $v_C$. It becomes more stable if $T_n$, $T_r$, $R_t$, and $C$ are decreased and $T_p$ is increased. This means that $C$ in the range of $\mu$F makes it more stable in comparison with $m$F. However, a bad case, a high-capacity capacitor, has been employed in this article to ensure the stability.

## IV. IMPORTANT EQUATIONS OF THE EV BC

### A. The Plants

The leg $Q_7 Q_8$ with its inductor can be described as

$$-d_B v_{\mathrm{dc}} + L_B \frac{di_B}{dt} + R_B i_B + v_B = 0 \quad (3)$$

and in Laplace domain as

$$i_B = \frac{v_{\mathrm{dc}}}{L_B s + R_B} d_B - \frac{1}{L_B s + R_B} v_B. \quad (4)$$

Here, $v_B$ is considered as disturbance and $d_B$ is considered as control signal. $d_B$ is duty cycle of the upper switch $Q_7$ and $1 - d_{\mathrm{dc}}$ is duty cycle of the lower switch $Q_8$. $R_B$ is the sum of ON-state resistance of the switches and internal resistance of the inductor.

The leg $Q_7 Q_8$ with its inductor also works as an independent voltage source and can be described as

$$i_B - i'_{\mathrm{ext}} = C' \frac{dv_B}{dt} \quad (5)$$

with (3) and in Laplace domain as

$$v_B = \frac{v_{\mathrm{dc}} d_B}{L_B C' s^2 + R_B C' s + 1} - \frac{(L_B s + R_B)\, i'_{\mathrm{ext}}}{L_B C' s^2 + R_B C' s + 1}. \quad (6)$$

Here, $i'_{\mathrm{ext}}$ is considered as disturbance and $d_B$ is considered as control signal. Due to similarity between the legs $Q_9 Q_{10}$ and $Q_7 Q_8$, the equations of the leg $Q_9 Q_{10}$ are not stated.

### B. Efficiency

The power electronic topology proposed in Fig. 1 has five IGBT legs connected to each other in a definite way. So, it is necessary to discuss the non-ideal behavior of one IGBT leg. As discussed in [33], the non-ideal averaged model can be regarded as the ideal averaged model supplemented by the ON-state resistance of one IGBT connected in series with the internal resistance of the inductor of the leg ($R_{\mathrm{co}}$) and an independent current source connected in parallel with dc link for each IGBT leg ($I_{\mathrm{sw}}$). The former represents the conduction losses and the latter represents the switching losses. Now, they are expressed for a single IGBT leg as [33]

$$P_{\mathrm{sw}} = v_{\mathrm{dc}} \times I_{\mathrm{sw}} = v_{\mathrm{dc}} (Q_{\mathrm{rr}} + Q_{\mathrm{tc}}) f_{\mathrm{sw}}, \quad (7)$$

$$P_{\mathrm{co}} = R_{\mathrm{co}} \times i^2 \quad (8)$$

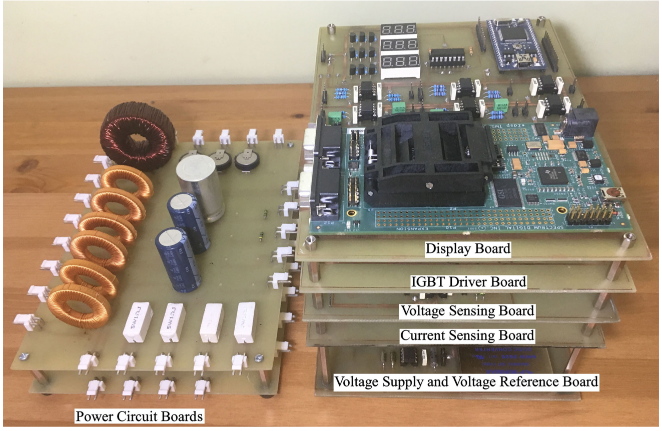

Fig. 4. Practical setup.

TABLE II
EXPERIMENTAL AND SIMULATION PARAMETERS

| Parameter | | Per Unit | Parameter | |
|---|---|---|---|---|
| $P_b$ | 16.8 W | 1 | $f_{sw}$ | 20 kHz |
| $v_b$ | 16.8 V | 1 | $T_p$ $T_n$ $T_r$ | 300 20 80 ms |
| $i_b$ | 1 A | 1 | $k_p$ $k_i$ | 2 7676.8 |
| $I_0$ | 1 A | 1.000 | $k'_p$ $k'_i$ | 2 7676.8 |
| $V_0$ | 16.8 V | 1.000 | $k''_i$ $k''_p$ | 0.4 1535.4 |
| $R_C$ | 7.68 Ω | 0.457 | $\tau_f$ | 1/(80000) s |
| $R_B$ | 7.68 Ω | 0.457 | $\tau'_f$ | 1/(100000) s |
| $R_t$ | 0.45 Ω | 0.027 | $C$ $C'$ | 330 0.2 mF |
| $v_{oc}$ | 16.6 V | 0.988 | $L_B$ | 2 mH |
| $v^*_{DC}$ | 24 V | 1.429 | $L_C$ | 2 mH |

| Parameter | | Per Unit | Parameter | | Per Unit |
|---|---|---|---|---|---|
| $P_b$ | 10500 W | 1 | $v_{oc}$ | 415 | 0.988 |
| $v_b$ | 420 V | 1 | $v_s$ | 240 V | 0.757 |
| $i_b$ | 25 A | 1 | $I_0$ | 25 A | 1.000 |
| $V_0$ | 420 V | 1.000 | $v^*_{DC}$ | 600 V | 1.429 |

where $Q_{\mathrm{rr}}$ and $Q_{\mathrm{tc}}$ are, respectively, the tailing and reverse recovery currents [33] and $i$ is the current flowing through the inductor. Obviously, $P_{\mathrm{sw}}$ and $P_{\mathrm{co}}$ can be calculated for all five IGBT legs. Therefore, the efficiency can be calculated as

$$E = \frac{P_0 - \sum_{j=1}^{j=5} P^j_{\mathrm{co}} - 5 I_{\mathrm{sw}} v_{\mathrm{dc}}}{P_0} \quad (9)$$

where $P_0$ equals $P_t$ in charging mode and $P_B$ in discharging mode. The input power is $P_t$ and the output power is $P_B$ in charging mode and vice versa in discharging mode. $P^j_{\mathrm{co}}$ is the conduction losses in the leg number $j$. Since $P_{\mathrm{sw}}$ only depends on the characteristics of the switches according to (7), it is the same for all the five IGBT legs.

## V. RESULTS

The proposed system in Fig. 1 has been simulated in MATLAB Simulink. On the other hand, the dc–dc stage in Fig. 1 with a kind of dc–ac converter has been implemented in practice as shown in Fig. 4. Table II shows the parameters of the small-scale and the main prototypes, respectively. $P_b$, $v_b$, and $i_b$ are the bases. The voltage and current bases in Table II for the experimental system are exactly 25 times smaller than

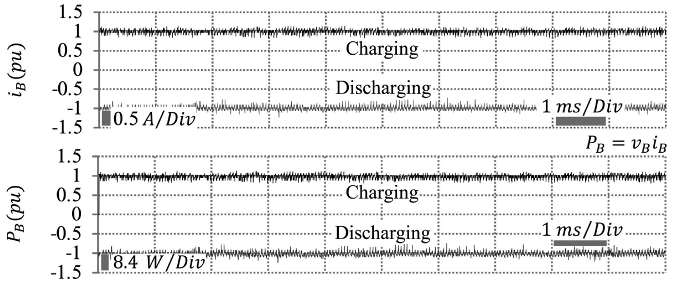

Fig. 5. Constant-current charging–discharging method.

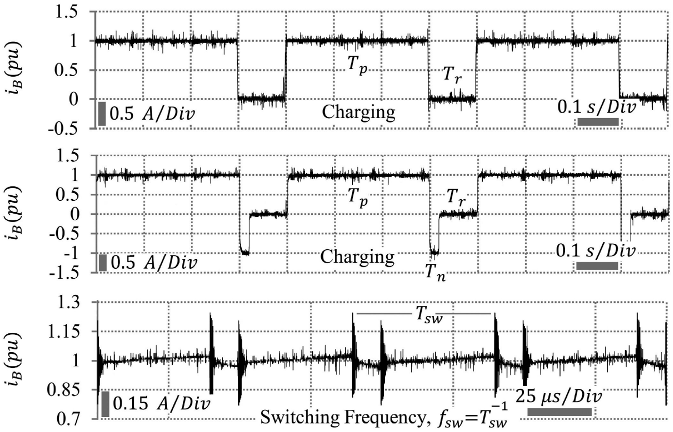

Fig. 6. Waveforms of the battery current when $T_n = 0$ and $T_n \neq 0$.

those for the simulation system. So, the power base in practice is $25 \times 25$ times smaller. A small prototype has been implemented in practice to decrease cost and avoid danger of electric shock. Also, the impedance bases in practice and simulation are exactly equal because both of the experimental voltage and current bases have been decreased equally 25 times, that is, exactly the same simulated system on a smaller scale in practice.

The experimental results are shown in Figs. 5–13. Fig. 5 shows the battery current and power. It confirms that the proposed system is able to charge and discharge the battery based on CC method. Figs. 6–13 show the important waveforms of some variables when it charges the battery based on pulse-current method without the negative part ($T_n = 0$) and with the negative part ($T_n \neq 0$). $T_p$ and $T_r$ last 300 and 80 ms, respectively, in all the waveforms. $T_n$ lasts 20  or 0 ms. $I_0$ equals 1 pu. All of the waveforms in Figs. 6–13 confirm that the proposed system successfully follows the sequences for the battery and the capacitor explained in Table I and Sections III-A and III-B.

The waveforms of the battery current $i_B$ in Fig. 6 have been shown two times on two different time scales. The waveforms on the long time scale, 0.1 s, confirm that it is charging based on pulse-current method with and without the negative part. The waveform on the short time scale, 50 $\mu$s, confirms that switching with the frequency of 20 kHz takes place.

Fig. 7 shows that the waveforms of the variable $i_B + i_{\text{in}}$. $i_{\text{in}}$ add a noticeable current to $i_B$ during $T_p$. In fact, this current charges the battery. $i_{\text{in}}$ flows only when $Q_{11}$ is ON. $Q_{11}$ is turned ON during only $T_p$ (see Table I again) to release the stored energy in the capacitor.

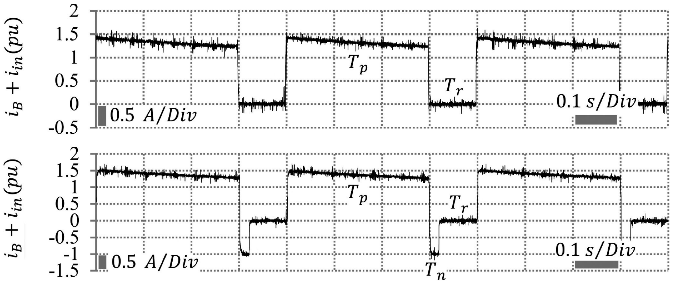

Fig. 7. Waveforms of the battery current with $i_{\text{in}}$ when $T_n = 0$ and $T_n \neq 0$.

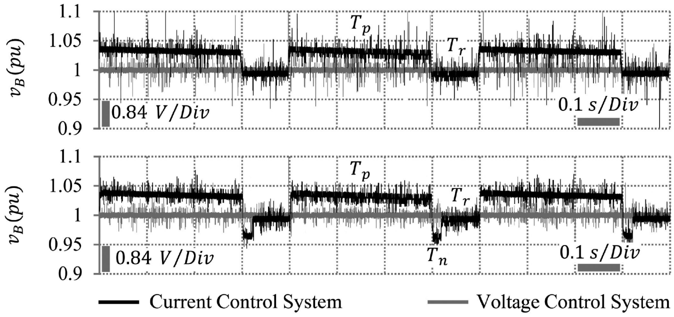

Fig. 8. Waveforms of the battery voltage when $T_n = 0$ and $T_n \neq 0$.

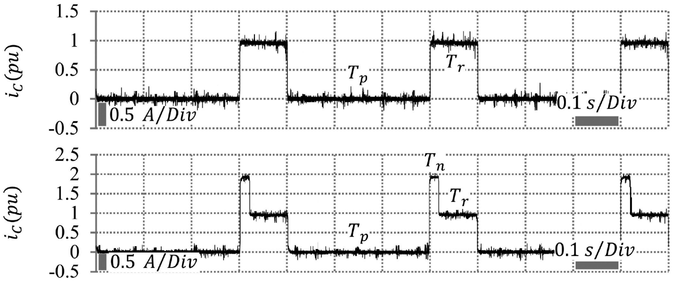

Fig. 9. Waveforms of the capacitor current when $T_n = 0$ and $T_n \neq 0$.

The waveforms of the battery voltage $v_B$ are shown in Fig. 8. $v_{\text{oc}}$ equals 16.6 V, 0.988 pu, when obtaining results. The maximum permissible voltage is 16.8 V and has been considered as the voltage base (see Table II).

The waveforms of the capacitor current $i_C$ are shown in Fig. 9. It confirms that the proposed system successfully follows the sequences of $i_C^*$ defined in the second row of Table I. It equals zero during $T_p$, $2I_0 v_{oc}/v_C$ during $T_n$, and $I_0 v_{oc}/v_C$ during $T_r$. In fact, the innovative allocation of $i_C^*$ and, in turn, $P_C$ in accordance with the rules defined in Table I resolves the power quality problem. In other words, $i_C$ and, in turn, $P_C$ make $P_B + P_C$ constant and continuous (smooth) during $T_p$, $T_n$, and $T_r$ (see Fig. 13).

Fig. 10 shows the waveforms of the capacitor voltage $v_C$. $v_C$ is stable and the amplitude of the ripple is approximately 0.05 pu. $v_{0p}, v_{0n}$, and $v_{0r}$ are greater than $v_B$ and less than $v_{\text{dc}}$ (1.429 pu). The behavior of $v_C$ has been fully explained in Sections III-B and III-C. $v_C$ increases during $T_n$ and $T_r$ because it receives power and decreases during $T_p$ because it delivers power. So, it

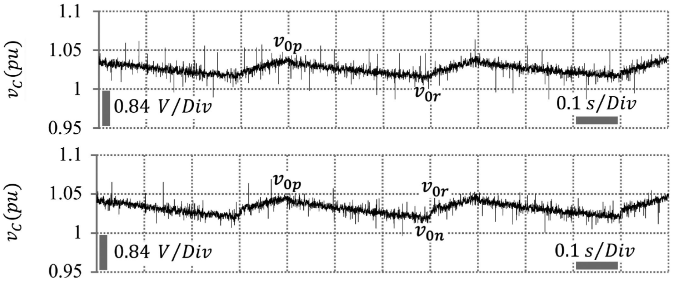

Fig. 10. Waveforms of the capacitor voltage when $T_n = 0$ and $T_n \neq 0$.

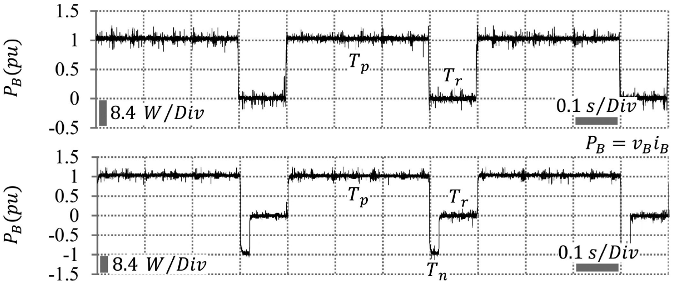

Fig. 11. Waveforms of the battery power when $T_n = 0$ and $T_n \neq 0$.

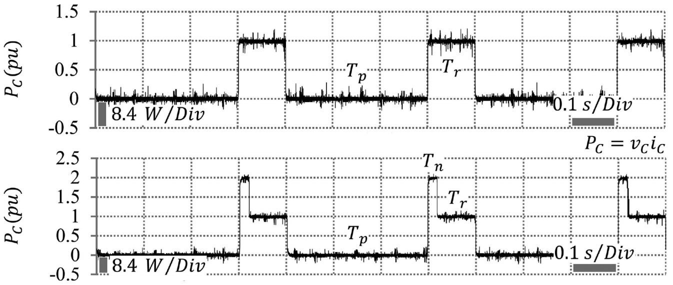

Fig. 12. Waveforms of the capacitor power when $T_n = 0$ and $T_n \neq 0$.

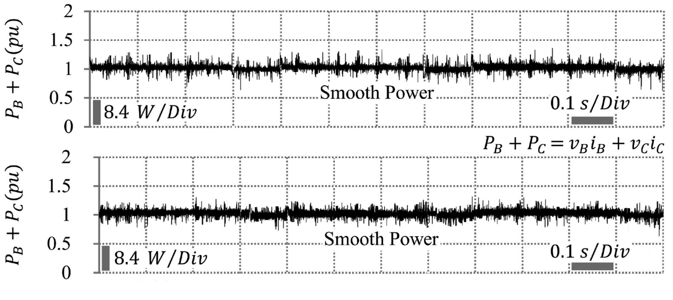

Fig. 13. Waveforms of the delivered power when $T_n = 0$ and $T_n \neq 0$.

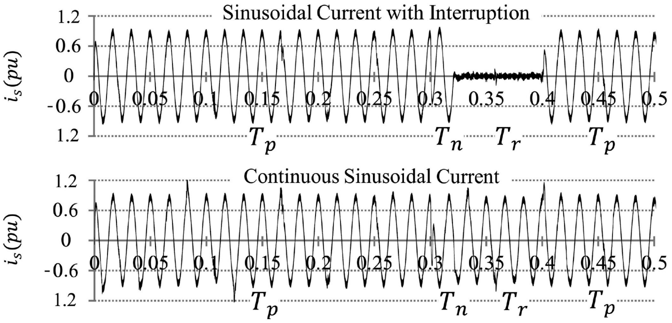

Fig. 14. AC-side terminal current for the two scenarios.

has the maximum value at the beginning of $T_p$ ($v_{0p}$) and has the minimum value at the beginning of $T_n$ ($v_{0n}$).

Figs. 11–13 show the most important waveforms of this article. $P_B$, $P_C$, and $P_B + P_C$ have the same patterns explained in Table I and Section III-B. Consider the following two scenarios. *First*, only the leg $Q_7Q_8$ is employed and the leg $Q_9Q_{10}$ is removed. Thus, $-P_s$ and $-P_{\text{ext}}$ approximately equal $P_B$. This condition describes the power quality problem in the pulse-current BCs proposed in the recent studies. *Second*, both the legs $Q_7Q_8$ and $Q_9Q_{10}$ are employed. Thus, $-P_s$ and $-P_{\text{ext}}$ approximately equal $P_B + P_C$. This condition contains the innovative concept presented in this article. In the *first* scenario, $P_B$ (shown in Fig. 11) is transferred. In the *second* scenario, $P_B + P_C$ (shown in Fig. 13) is transferred instead of $P_B$. $P_B + P_C$ has a continuous constant shape, while $P_B$ has interruption with the drastic power changes. The waveform of $P_B + P_C$ indicates that 1 pu smooth power is delivered to the dc–dc stage. Then, the battery is charged by $P_B$. In other words, the appropriate reference commands are innovatively allocated to the capacitor current $i_C$ and, in turn, $P_C$ in order to smoothen the intrinsic drastic power changes of $P_B$. Then, the smoothened power $P_B + P_C$ is transferred instead of the variable power $P_B$. The power quality problem of the first scenario is effectively solved in the second scenario.

Fig. 14 shows $i_s$ for the two mentioned scenarios. It depicts the bad effect of the drastic battery power changes at the ac-side terminal. The waveform of $i_s$ has interruption and three changes when the first scenario is considered. The waveform of $i_s$ has no noticeable changes and has a constant rms value when the second scenario is considered.

## VI. CONCLUSION

The results confirmed that the battery–capacitor configuration of the EV BC with its precisely designed control system successfully charges and discharges the battery based on pulse-current method with high capability to adjust the parameters and implement various algorithms. It can transfer smooth constant power from the battery to the microgrid and vice versa during V2G technology in the presence of the drastic battery power changes in pulse-current method. It can be used in many applications instead of dc–dc stage of various BCs such as the fuel-cell-powered BCs, the multi-output BCs, and the charging stations to share smooth constant power.

## REFERENCES

[1] Y. Gao, X. Zhang, Q. Cheng, B. Guo, and J. Yang, “Classification and review of the charging strategies for commercial Lithium-Ion batteries,” *IEEE Access*, vol. 7, pp. 43511–43524, 2019.

[2] J. Amanor-Boadu, A. Guiseppi-Elie, and E. Sánchez-Sinencio, “The impact of pulse charging parameters on the life cycle of lithium-ion polymer batteries,” *Energies*, vol. 11, no. 8, 2018, Art. no. 2162.

[3] L.-R. Chen, J.-J. Chen, N.-Y. Chu, and G.-Y. Han, “Current-pumped battery charger,” *IEEE Trans. Ind. Electron.*, vol. 55, no. 6, pp. 2482–2488, Jun. 2008.

[4] L.-R. Chen, C.-M. Young, N.-Y. Chu, and C.-S. Liu, “Phase-locked bidirectional converter with pulse charge function for 42-V/14-V dual-voltage power net,” *IEEE Trans. Ind. Electron.*, vol. 58, no. 5, pp. 2045–2048, May 2011.

[5] B. Purushothaman and U. Landau, “Rapid charging of Lithium-Ion batteries using pulsed currents a theoretical analysis,” *J. Electrochemical Soc.*, vol. 153, no. 3, pp. A533–A542, 2006.

[6] L.-R. Chen, N.-Y. Chu, C.-S. Wang, and R.-H. Liang, “Design of a reflex-based bidirectional converter with the energy recovery function,” *IEEE Trans. Ind. Electron.*, vol. 55, no. 8, pp. 3022–3029, Aug. 2008.

[7] H.-J. Chiu, L.-W. Lin, P.-L. Pan, and M.-H. Tseng, “A novel rapid charger for lead-acid batteries with energy recovery,” *IEEE Trans. Power Electron.*, vol. 21, no. 3, pp. 640–647, May 2006.

[8] C.-T. Tsai, Y.-C. Kuo, Y.-P. Kuo, and C.-T. Hsieh, “A reflex charger with ZVS and non-dissipative cells for photovoltaic energy conversion,” *Energies*, vol. 8, no. 2, pp. 1373–1389, 2015.

[9] J. Y. Yong, V. K. Ramachandaramurthy, K. M. Tan, and N. Mithulananthan, “A review on the state-of-the-art technologies of electric vehicle, its impacts and prospects,” *Renewable Sustain. Energy Rev.*, vol. 49, pp. 365–385, 2015.

[10] M. A. Monem *et al.*, “Lithium-Ion batteries: Evaluation study of different charging methodologies based on aging process,” *Appl. Energy*, vol. 152, pp. 143–155, 2015.

[11] J. Li, E. Murphy, J. Winnick, and P. A. Kohl, “The effects of pulse charging on cycling characteristics of commercial lithium-ion batteries,” *J. Power Sources*, vol. 102, no. 1-2, pp. 302–309, 2001.

[12] H.-I. Hsieh, C.-Y. Tsai, and G.-C. Hsieh, “Photovoltaic burp charge system on energy-saving configuration by smart charge management,” *IEEE Trans. Power Electron.*, vol. 29, no. 4, pp. 1777–1790, Apr. 2014.

[13] L.-R. Chen, “Design of duty-varied voltage pulse charger for improving Li-Ion battery-charging response,” *IEEE Trans. Ind. Electron.*, vol. 56, no. 2, pp. 480–487, Feb. 2009.

[14] L.-R. Chen, “A design of an optimal battery pulse charge system by frequency-varied technique,” *IEEE Trans. Ind. Electron.*, vol. 54, no. 1, pp. 398–405, Feb. 2007.

[15] J. M. Amanor-Boadu, M. A. Abouzied, and E. Sánchez-Sinencio, “An efficient and fast Li-Ion battery charging system using energy harvesting or conventional sources,” *IEEE Trans. Ind. Electron.*, vol. 65, no. 9, pp. 7383–7394, Sep. 2018.

[16] J. M. Amanor-Boadu, A. Guiseppi-Elie, and E. Sánchez-Sinencio, “Search for optimal pulse charging parameters for Li-ion polymer batteries using Taguchi orthogonal arrays,” *IEEE Trans. Ind. Electron.*, vol. 65, no. 11, pp. 8982–8992, Nov. 2018.

[17] L.-R. Chen, S.-L. Wu, D.-T. Shieh, and T.-R. Chen, “Sinusoidal-ripple-current charging strategy and optimal charging frequency study for Li-ion batteries,” *IEEE Trans. Ind. Electron.*, vol. 60, no. 1, pp. 88–97, Jan. 2013.

[18] L.-R. Chen, J.-J. Chen, C.-M. Ho, S.-L. Wu, and D.-T. Shieh, “Improvement of Li-ion battery discharging performance by pulse and sinusoidal current strategies,” *IEEE Trans. Ind. Electron.*, vol. 60, no. 12, pp. 5620–5628, Dec. 2013.

[19] M. Tabari and A. Yazdani, “Stability of a DC distribution system for power system integration of plug-in hybrid electric vehicles,” *IEEE Trans. Smart Grid*, vol. 5, no. 5, pp. 2564–2573, Sep. 2014.

[20] Z. Jiang and R. A. Dougal, “Control strategies for active power sharing in a fuel-cell-powered battery-charging station,” *IEEE Trans. Industry Appl.*, vol. 40, no. 3, pp. 917–924, May/Jun. 2004.

[21] Z. Jiang and R. A. Dougal, “Synergetic control of power converters for pulse current charging of advanced batteries from a fuel cell power source,” *IEEE Trans. Power Electron.*, vol. 19, no. 4, pp. 1140–1150, Jul. 2004.

[22] M. Kesler, M. C. Kisacikoglu, and L. M. Tolbert, “Vehicle-to-grid reactive power operation using plug-in electric vehicle bidirectional offboard charger,” *IEEE Trans. Ind. Electron.*, vol. 61, no. 12, pp. 6778–6784, Dec. 2014.

[23] M. C. Kisacikoglu, M. Kesler, and L. M. Tolbert, “Single-phase on-board bidirectional PEV charger for V2G reactive power operation,” *IEEE Trans. Smart Grid*, vol. 6, no. 2, pp. 767–775, Mar. 2015.

[24] P.-J. Liu and C.-H. Yen, “A fast-charging switching-based charger with adaptive hybrid duty cycle control for multiple batteries,” *IEEE Trans. Power Electron.*, vol. 32, no. 3, pp. 1975–1983, Mar. 2017.

[25] J. Wang and C. Chuang, “Design considerations of microprocessor-controlled multiphase battery charger with fast-charging strategy,” *IET Electric Power Appl.*, vol. 1, no. 2, pp. 143–152, 2007.

[26] M. Abdel-Monem, K. Trad, N. Omar, O. Hegazy, P. Van den Bossche, and J. Van Mierlo, “Influence analysis of static and dynamic fast-charging current profiles on ageing performance of commercial lithium-ion batteries,” *Energy*, vol. 120, pp. 179–191, 2017.

[27] J. A. A. Qahouq and Z. Xia, “Single-perturbation-cycle online battery impedance spectrum measurement method with closed-loop control of power converter,” *IEEE Trans. Ind. Electron.*, vol. 64, no. 9, pp. 7019–7029, Sep. 2017.

[28] A. Lasia, “Electrochemical impedance spectroscopy and its applications,” in *Modern Aspects of Electrochemistry*. Berlin, Germany: Springer, 2002, pp. 143–248.

[29] J. Sihvo, D.-I. Stroe, T. Messo, and T. Roinila, “A fast approach for battery impedance identification using pseudo random sequence (PRS) signals,” *IEEE Trans. Power Electron.*, vol. 35, no. 3, pp. 2548–2557, Mar. 2020.

[30] M. A. Varnosfaderani and D. Strickland, “A comparison of online electrochemical spectroscopy impedance estimation of batteries,” *IEEE Access*, vol. 6, pp. 23668–23677, 2018.

[31] W. Huang and J. A. A. Qahouq, “An online battery impedance measurement method using DC-DC power converter control,” *IEEE Trans. Ind. Electron.*, vol. 61, no. 11, pp. 5987–5995, Nov. 2014.

[32] Y.-D. Lee, S.-Y. Park, and S.-B. Han, “Online embedded impedance measurement using high-power battery charger,” *IEEE Trans. Ind. Appl.*, vol. 51, no. 1, pp. 498–508, Jan./Feb. 2015.

[33] A. Yazdani and R. Iravani, *Voltage-Sourced Converters in Power Systems*, vol. 34. Hoboken, NJ, USA: Wiley, 2010.

[34] A. Khaligh and Z. Li, “Battery, ultracapacitor, fuel cell, and hybrid energy storage systems for electric, hybrid electric, fuel cell, and plug-in hybrid electric vehicles: State of the art,” *IEEE Trans. Veh. Technol.*, vol. 59, no. 6, pp. 2806–2814, Jul. 2010.